A thalamic hub of action cues coordinates early visual processing and perception

T. Vega-Zuniga[1]†*, A. Sumser[1,2]†, O. Symonova[1], P. Koppensteiner[1], F. H. Schmidt[1], M. Joesch[1]*

[1] Institute of Science and Technology Austria; Am Campus 1, 3400 Klosterneuburg, Austria.

[2] Division of Neuroscience, Faculty of Biology, LMU Munich, 82152 Martinsried, Germany

* Corresponding authors. Email: tomas.vegazuniga@ist.ac.at; maxjosch@ist.ac.at

† These authors contributed equally to this work

Abstract:

Distinguishing between sensory experiences elicited by external stimuli and an animal's own actions is critical for accurate perception. However, the diversity of behaviors and their complex influences on the senses make this distinction challenging. Here, we show that a combination of self-motion cues modulates visual processing in the superficial superior colliculus (sSC), the brain's first visual relay. We uncovered a projection from the ventral lateral geniculate nucleus to the sSC in mice that functions as a corollary discharge hub, conveying inhibitory signals about translational optic flow and motor dynamics, including saccades, locomotion, and pupil size. Activation of this projection potently dampens visual responses and concurrently drives corresponding motor actions that resemble motor prediction errors; suppression disrupts action-specific visual perception. Our results show that visual signals undergo continuous refinement at the earliest stages through the convergence of self-motion information, ensuring accurate visual perception and visuomotor control.

Main Text:

Vision is constantly challenged by the animal's movements (*1*). At the sensory periphery, the origins of the sensory perturbations are ambiguous - they are indistinguishable between changes in the environment (exafferent information) or as a consequence of the animal's movement (reafferent information) (Fig. 1A). Yet, this distinction must become operational to ensure that animals experience a behaviorally coherent perception while moving through the world (*2*). The variety and dynamic nature of vertebrate behavior depend on complex brain-body coordination carved throughout evolution. This behavioral enrichment coevolved with an intricate battery of neural mechanisms to actively compensate for displacement of the visual world while moving. These mechanisms include the coordination of multiple senses, e.g., visual and vestibular modalities (*3*), and require an internal representation of movement commands known as corollary discharge (CD) (Fig. 1B). The main function of CD is to filter out reafferent signals, allowing precise sensorimotor transformations needed to effectively infer the structure of the external world (*1*, *4*) and experience perceptual continuity (*5*). One prominent example is saccadic suppression in the primate oculomotor system, where CD signals the direction and intensity of a forthcoming saccadic eye movement to suppress the perception of motion-induced blur (*5*). However, motion can affect visual processing in myriad ways, making effective estimation of the reafferent signal complex. This complexity is particularly evident when these corrections are distributed throughout the brain, as observed in mammals, where CD associated with visual processing has been found primarily in thalamic and cortical regions (*1*, *6*).

The superior colliculus (SC), a prominent midbrain hub conserved across vertebrates (*7*), plays a critical role in visual sensorimotor transformations, including humans (*8–10*). The output of the SC has been associated with CD and has been largely studied in the context of saccadic suppression (*6*). The current view is that, at least in primates, intermediate layers of the SC send ascending motor commands to the medial dorsal nucleus of the thalamus and then to the frontal eye fields in the cortex, an area known to contribute to voluntary saccades (*6*). However, the SC has been implicated in many different visuomotor processes, ranging from visual perception to cognition (*11*), and some of these processes have been shown to be independent of cortical function (*12*, *13*). Thus, to ensure proper visual perception and visuomotor control via the SC, the SC may not only provide the motor signals required to generate the CD, but would also require processes that allow correction of a range of self-motion-induced visual distortions.

CD signals can take many forms, such as compensation, attenuation, or suppression (*14*). The last two are the best-known CD signals, which are primarily mediated by inhibitory inputs. Accordingly, distinct SC layers are targeted differentially by long-range inhibitory projection from various brain areas (*15–18*). Among these pathways, the vLGN/IGL complex, a retino-receptive subcortical region in the lateral thalamus (*19*), seems well-placed to perform such operations. Most neurons are GABAergic (*15*, *16*), their connections cover all major parts of the visual brain (for details, see (*20*)), and they are involved in a wide variety of tasks - from visual threat response behavior (*15*, *16*), circadian rhythms (*20*, *21*), nocifensive behavior (*22*),

chromatic discrimination (*23*), optokinetic reflex (*24*) to visuomotor control (*20*, *21*, *25–28*). Here, we show that the inhibitory vLGN/IGL complex strongly inhibits all neurons in the superficial SC and modulates visual responses *in vivo*. This pathway simultaneously transmits visually evoked forward translation-like optic flow patterns and signals ongoing behaviors with visual effects, such as locomotion, saccades, and pupil dilation. Surprisingly, optogenetic stimulation produces concordant stereotyped movements, and its targeted suppression disrupts visual behaviors that require integration of vision and movement. Our data show that the vLGN/IGL complex plays a critical role in visuomotor transformations by suppressing unwanted visual signals from a combination of behaviors at the first visual relay.

Strong vLGN/IGL inhibitory projection to the superficial superior colliculus

The vLGN/IGL complex is a retino-recipient thalamic nucleus composed of mainly inhibitory neurons (*15*, *16*). To determine the brain-wide and SC-specific projections that arise from the vLGN, we performed anterograde and retrograde labeling experiments. First, we infected the visual cortex (VC) with AAV1-CamKII-Cre, a viral serotype known to cross synapses anterogradely, to infect projection neurons and their recipient neurons in the thalamus, which includes the vLGN and the dorsal LGN (dLGN) (Fig. 1C, D - red nuclei). We then specifically infected the visual thalamus with a Cre-dependent GFP reporter virus. We did not observe any retrogradely green labeled L5 pyramidal cells in the VC (Fig. S1), only vLGN and dLGN neurons were labeled (Fig. 1D). We observed a pronounced projection to the superficial SC (sSC) (Fig. 1E, F), a major retinorecipient structure in the vertebrate brain. This projection was directed to the lower layers of the sSC, where most somata are located (*29*), suggesting that these inputs could exert a prominent modulatory influence. We also observed, but to a lesser extent, a previously reported projection to the intermediate layers (*15*, *16*) (Fig. 1E) and several brain-wide projection patterns to a range of subcortical areas, targeting the thalamus (lateral posterior nucleus, nucleus reuniens, contralateral vLGN, lateral habenula), midbrain (posterior pretectal nucleus, anterior pretectal nucleus, olivary pretectal nucleus, periaqueductal gray), and hindbrain (pons, inferior olive) (Fig. S2). These projection patterns can be recapitulated by infecting Gad2^{+} cells in the vLGN/IGL (Fig. S3) (*30*). To confirm the specificity of the vLGN to sSC projection, we next used the highly neurotropic N2c rabies virus vectors (*31*) to retrogradely label the presynaptic neurons of three sSC-specific driver lines that label wide-field, narrow-field, and a mixture of sSC neurons using the Ntsr1-GN209, Grp, and Rorb-Cre lines, respectively (Fig. 1G)(*29*). In all cases, we observed strong vLGN labeling, with few or no labeled cells in the IGL, and no labeled neurons in the dLGN (Fig. 1H-J). These results demonstrate that the vLGN, like the IGL (*16*), has a pronounced projection to the ipsilateral sSC. Next, we determined the synaptic properties between vLGN/IGL and the sSC. We performed *in vitro* whole-cell recordings of sSC neurons together with optogenetic stimulation of Gad2^{+} vLGN/IGL terminals expressing channelrhodopsin-2 (ChR2) (Fig. 1K-N). First, we characterized the physiological properties of each cell performing current injections as previously done (*29*), defining distinct cell types based on their intrinsic spiking properties (*29*) (Fig. 1M). In neurons that fired spontaneously, optogenetic activation had a strong suppressive effect (Fig. 1N), and a large inhibitory postsynaptic current (IPSC) was measured

in all cells, regardless of their type (Fig. 1O, P). These currents were mediated by $GABA_A$ receptors, as shown pharmacologically with bicuculline (Fig. 1O, P). In conclusion, we show that the vLGN/IGL complex is well-positioned to exert a strong modulatory influence on the first visual relay.

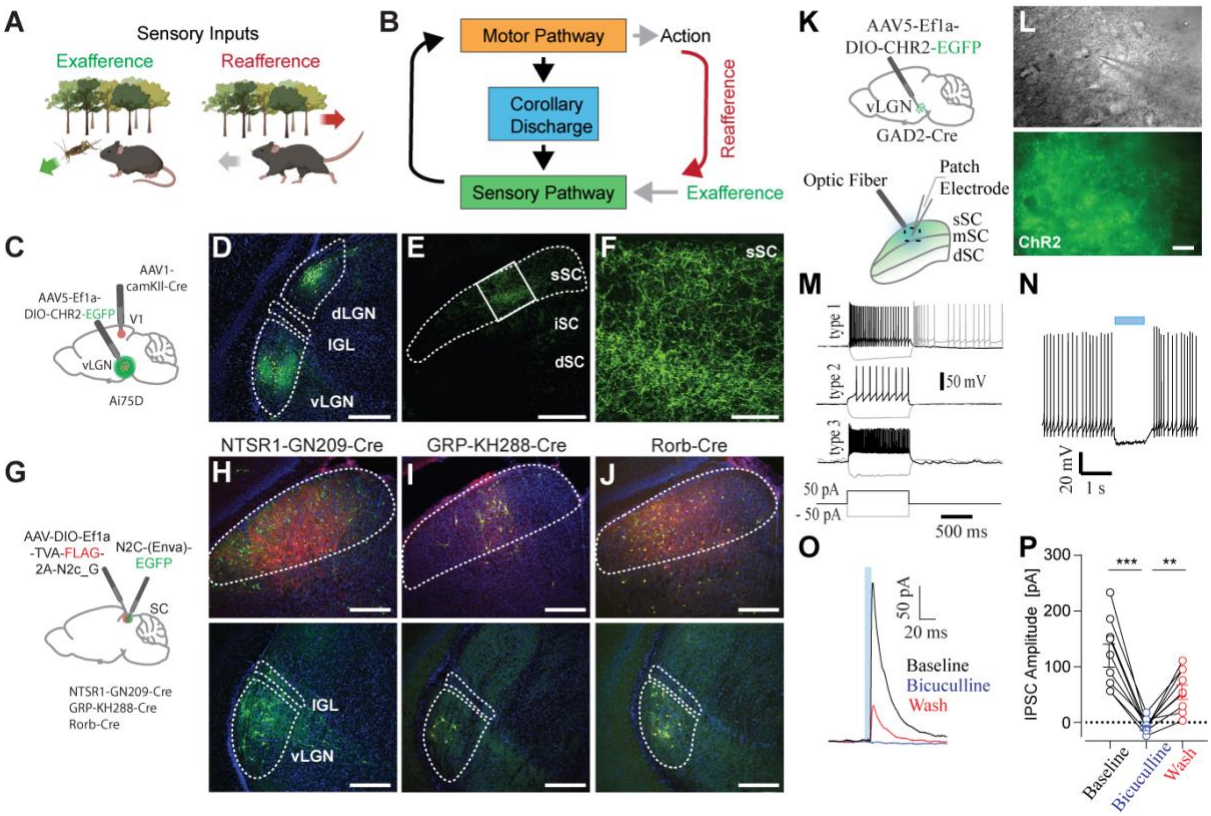

Fig. 1 vLGN/IGL strongly inhibits the superficial SC. **A**, Schematic showing the difference between external visual input (exafference, green arrow) and visual input generated by the animal's own motion (reafference, red arrow). **B**, Schematic showing a sensorimotor circuit with a motor-copy signal, known as a corollary discharge (CD, blue) bridging a sensory pathway (green) and a motor pathway (orange). **C**, Brain schematic showing the location of anterograde transsynaptic vector injection. Primary visual cortex (V1, red dot) and ventral lateral geniculate nucleus (vLGN, green dot). **D**, Brain section showing nuclear tdTomato and channelrhodopsin (ChR2)-EGFP expression after Cre-dependent vector injection in the vLGN. **E**, Expression of ChR2 in vLGN terminals in the superficial superior colliculus (sSC). **F**, Close-up of sSC (box in **E**). **G**, Brain schematic showing the location of retrograde transsynaptic vector injections in the sSC. **H-J**, Coronal brain sections of the three transgenic lines. Top: sSC with starter vector expression in red. Bottom: Transsynaptic expression of the pseudorabies vector in the vLGN. **K**, Schematic brain showing a vLGN injection of ChR2 and subsequent patch clamp recordings in the sSC. **L**, Image showing the patch area in the sSC (top) and the corresponding ChR2-expressing vLGN terminals (bottom). **M**, Intrinsic firing properties of sSC cell types in response to a current step. **N**, Current-clamp recording of spontaneous activity of sSC cells suppressed by 20 Hz optogenetic stimulation. **O**, Voltage-clamp recording of an sSC neuron. Inhibitory currents induced by optogenetics are reversibly blocked by bicuculline (20 µM). **P**, IPSC amplitude of all recorded neurons in the presence of bicuculline and subsequent wash. All scale bars: 100 µm, but **F**: 50 µm.

***In vivo* suppression of visual responses in the superior colliculus.**

To explore the modulatory influence of vLGN on visual processing, we simultaneously recorded visually-evoked responses across different layers of the SC, using 32-channel silicon probes in head-fixed awake-behaving mice, and optogenetically activated the vLGN/IGL complex (Fig. 2A, B). For this purpose, we used the same viral delivery approach and Gad2-cre mice as for *in vitro* physiology (Fig.1K), subsequently implanting an optical **λ**-fiber to the ventral thalamus for optogenetic stimulation (Fig.2C, D). First, we determined the recording depth using visually evoked responses and current source density (CSD) analysis (Fig. 2E, left), which aligned with the histological reconstruction of the probe position marked with DiI staining (Fig. 2D). Next, we repeated the same experiment optogenetically to compare the relative influence of the inhibitory thalamic projection and observed an inversion of the current source reflecting the inhibitory nature of the thalamic projection (Fig. 2E, right). The response depth of the visual and optogenetic responses overlapped, but the optogenetics CSDs reached further to the intermediate layers as expected from the anatomical projection (Fig. 2F). Visual responses peaked at ~ 60 ms after the visual and optogenetic-driven activity due to the speed of the phototransduction, whereas optogenetic responses had a peak-latency of a few milliseconds (Fig. 2G). To determine how these pronounced inhibitory dynamics influence visual responses in the sSC, we combined 1 s small visual flashes (10 ° of visual angle) centered in the receptive fields of the recorded sSC interneurons with interspersed and randomized vLGN/IGL optogenetic stimulation (Fig. 2H). Optogenetic activation could suppress both baseline firing and visually evoked responses, even though visual response properties were diverse. Variation of effect strength is expected, given that it depends on the infection efficacy, as well as the relative retinotopic alignment of the optic fiber and recording electrode. Thus, we determined the population of neurons that were visually and optogenetically responsive using parameter-free tests of stimulus-evoked responsiveness to study the interactions directly (see methods). 69 % of all recorded neurons were visually responsive, from which 75 % were responsive to optogenetic stimulation. On average, this population showed a mild modulation of the baseline firing (Fig. 2I, middle, J) but a strong and effective suppression of visually evoked responses (Fig. 2I, right, K), lowering the maximal firing rate by ~60 % (Fig. 2I, bottom), in line with recent reports (*32*). In rare occasions, optogenetics had a net excitatory effect after an initial suppression, likely due to network interactions. To determine the kinetics of the inhibition, we repeated the experiments shown in (Fig. 2H), but with shorter (200 ms) optogenetic and visual stimulation. vLGN/IGL suppression was largely transient, being strongest when visual and optogenetic stimuli overlapped, and lasted for about 100 ms after the offset of the optogenetic stimulus (Fig. 2L). Finally, since the relative timing of the first spike has been shown to be an effective retinal code (*33*), we wondered if the feedforward suppression would modulate spike timing precision. We tested the spike-timing precision, subselecting neurons that had no complete suppression and compared the spike time of the first spike. On average, the optogenetic stimulation had only a small effect, delaying the first spike by a median of 3 ms (Fig. 2M). Consistent with the spread of the vLGN projection to lower SC layers (*15*, *16*), we observed similar suppression in deeper SC layers (Fig. S4). Overall, this

data shows that the vLGN/IGL complex acts as a feedforward inhibitory hub capable of strongly modulating the magnitude of visual responses across the sSC.

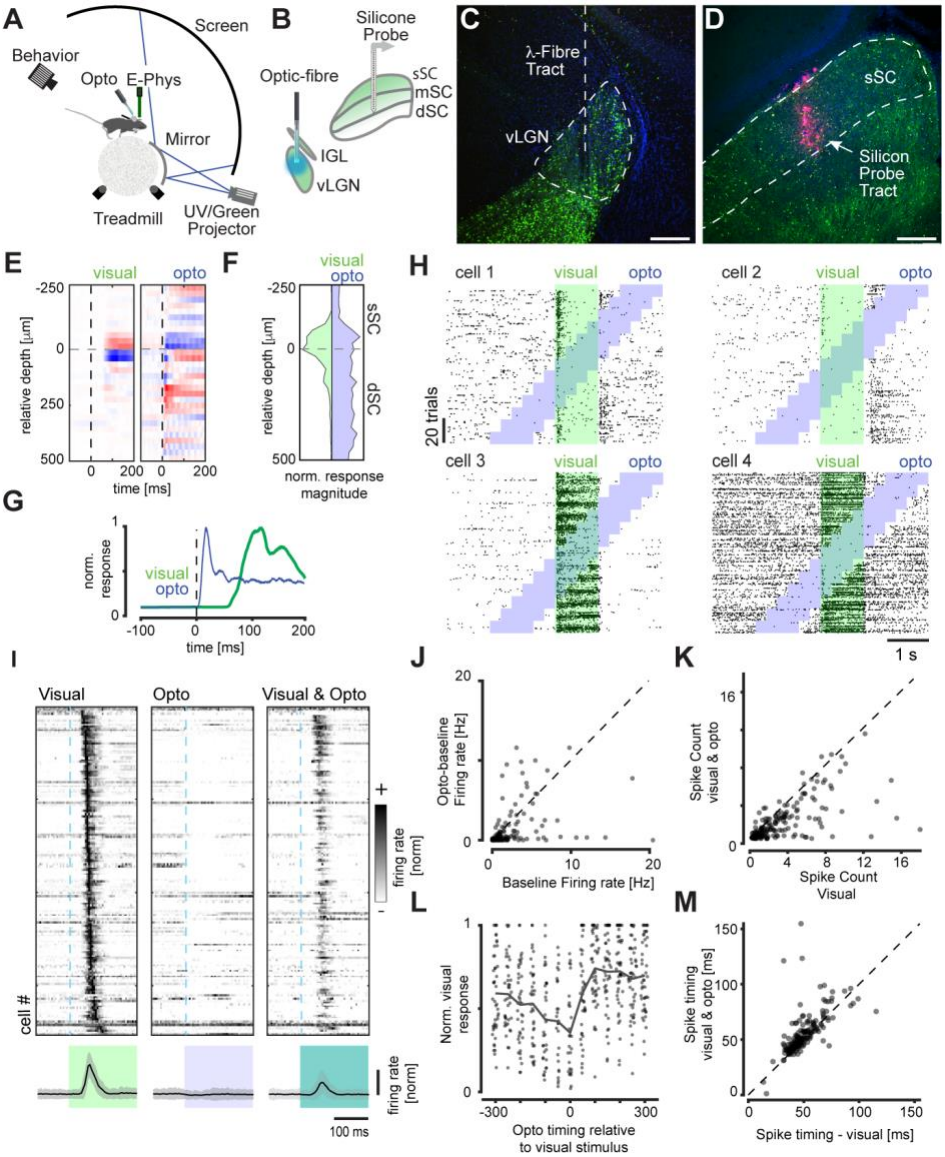

Fig. 2 vLGN/IGL complex suppresses visual responses *in vivo*. **A**, Schematic of the electrophysiology setup, with mice head restrained while running on a spherical treadmill and visual stimulation on a panoramic dome. **B**, Schematic of ChR2 virus infection in Gad2^{+} neurons in the vLGN/IGL complex and placement of the recording electrode. **C**, Confocal image of the vLGN and the optical fiber track for optogenetics. **D**, Confocal image of the SC with the DiI-labeled track of the recording electrode. **E**, Current source density (CSD) analysis for visual flash stimuli (left) and optogenetic stimulation (right). Black vertical dashed line indicates stimulus onset. **F**, Average contours of normalized CSD over depth. **G**, Temporal profile of CSD activation. **H**, Spike raster plots of visually and optogenetically responsive sample neurons of the superficial SC (sSC). Visual stimulus epochs (green) are interleaved with optogenetic stimulation (blue). **I**, Sorted and normalized firing responses of sSC neurons to visual, optogenetic, and combined stimulation (top) with their respective population mean responses (bottom, mean +/- STD). **J-K**, Quantification of optogenetic baseline and visually evoked activity suppression. **L**, Quantification of the duration of inhibition kinetics. **M**, Analysis of the optogenetic influence on visually evoked spike timing. Scale bars: 100 µm.

vLGN/IGL is a central hub for corollary discharge.

To investigate the scenarios in which the vLGN/IGL complex modulates sSC visual processing, we analyzed the response properties of vLGN/IGL axon terminals in the sSC (see Fig. 3A). We introduced the calcium indicator axon-GCaMP6s (*34*) into Gad2$^+$ cells by infecting the vLGN (Fig. 3B-D, n = 4 mice), resulting in homogeneous GCaMP expression throughout the SC (Fig. 3C). Subsequent implantation of a cranial window over the superior colliculus allowed observation of activity in axonal terminals from the thalamus using two-photon calcium imaging in awake, behaving mice. The field of view varied between recordings, ranging from 0.2 to 1.8 mm^2 (median = 0.7 mm^2) of the SC surface. In addition, retinal terminals in the SC were recorded to qualitatively compare their response characteristics (Fig. S5), using a similar field of view of 0.1 to 1.6 mm^2 (median = 0.7 mm^2). We used a variety of visual stimuli to assess bouton response properties, with interleaved periods of uniform light level (gray screen) to assess the activity associated with spontaneous animal behavior.

First, we tested bouton responses to a "chirp" stimulus (*35*), which involves full-field modulations of light intensity (Fig. 3E). Among all vLGN/IGL boutons meeting the inclusion criteria (see methods), some showed robust responses to full-field flashes, as previously reported (*36*). However, the majority showed their most pronounced responses to rapid frequency modulations. Retinal boutons, on the other hand, showed a wider range of feature selectivities to the stimulus (Fig. S5E). Next, we determined directional selectivity to full-field moving grating stimuli, which in vLGN/IGL boutons showed a striking preference for temporal grating motion (Fig. 3F), as would be seen during forward locomotion. In contrast to retinal ganglion cell (RGC) responses (*37*), the use of a random checkerboard or sparse dot stimulus did not yield robust receptive field estimates for vLGN/IGL boutons. Nevertheless, we wanted to determine the retinotopic organization of the terminals in the sSC. To this end, we tested whether a visual bar moving slowly (22.5 °/sec) across the visual field elicited sequential activations that were anatomically localized. Retinal synapses showed a distinct spatial representation (Fig. S5G), whereas vLGN/IGL terminals showed global responses when a bar crossed visual space, consistent with electrophysiological data indicating large spatial receptive fields (*36*) (Fig. 3G). Overall, approximately half (48 %) of the included vLGN/IGL boutons (RGC: 93 %) responded significantly ($p < 0.01$, Bonferroni corrected) to at least one of the visual stimuli presented (Fig. 3H).

During gray screen periods, activity in retinal boutons was weak and sparse (Fig. S5I), whereas calcium signals in vLGN/IGL boutons varied strongly (Fig. 3I). Compared to the retinal terminals, vLGN/IGL boutons were highly synchronously active (on average 18% variance explained by population mean for vLGN/IGL, 3% for RGCs; Fig. S6A, B), indicating that the vLGN is transmitting a global signal. We found that activity peaks often coincided with locomotor bursts and thus compared vLGN/IGL bouton signals with behavioral parameters. Indeed, many vLGN/IGL boutons significantly changed their activity around locomotion onset (19 %) and saccade onset (42 %) (Fig. 3J, K). Of the ~220,000 bouton population included, 36 % were significantly correlated with locomotor speed and 62 % with alertness as indicated by pupil size ($p < 0.001$, shuffle test). Confirming previous results (*38*), retinal inputs to the

sSC were also modulated by behavior during gray periods, with a quarter of retinal boutons significantly affected by at least one of the measured behavioral parameters (Fig. S5I-L). However, vLGN/IGL bouton activity was coupled to behavior to a much greater extent and proportion, with 80 % of boutons significantly and mostly positively modulated by behavior (Fig. 3L, Fig. S5L), in stark contrast to retinal axons (Fig. 3J, Fig. S5). The timing of the vLGN/IGL is either coupled instantaneously or precedes behavioral changes (Fig. S6C-E), making it well positioned to act as corrective feedback of reafferent signals. Since the dynamics of locomotion and pupil size can be coupled (median correlation across recordings c = 0.24, n = 67, Fig. S6F), we next tested whether vLGN bouton activity coupling to each behavior is independent. We compared the difference of correlation of vLGN/IGL and retinal activity with pupil size overall and during resting epochs only. We found that without locomotion pupil size correlations were significantly lower for both bouton populations, but to a far larger extent in vLGN/IGL boutons (effect size r = 0.54) than RGC boutons (r = 0.09), indicating that locomotion and pupil dynamics exert an independent influence on vLGN/IGL boutons (Fig. S6F-I). In conclusion, the vLGN/IGL to sSC projection is activated by cross-modal, visual and behavioral, providing a potent inhibition of visual signaling when changes in the retinal image are expected to occur due to self-motion.

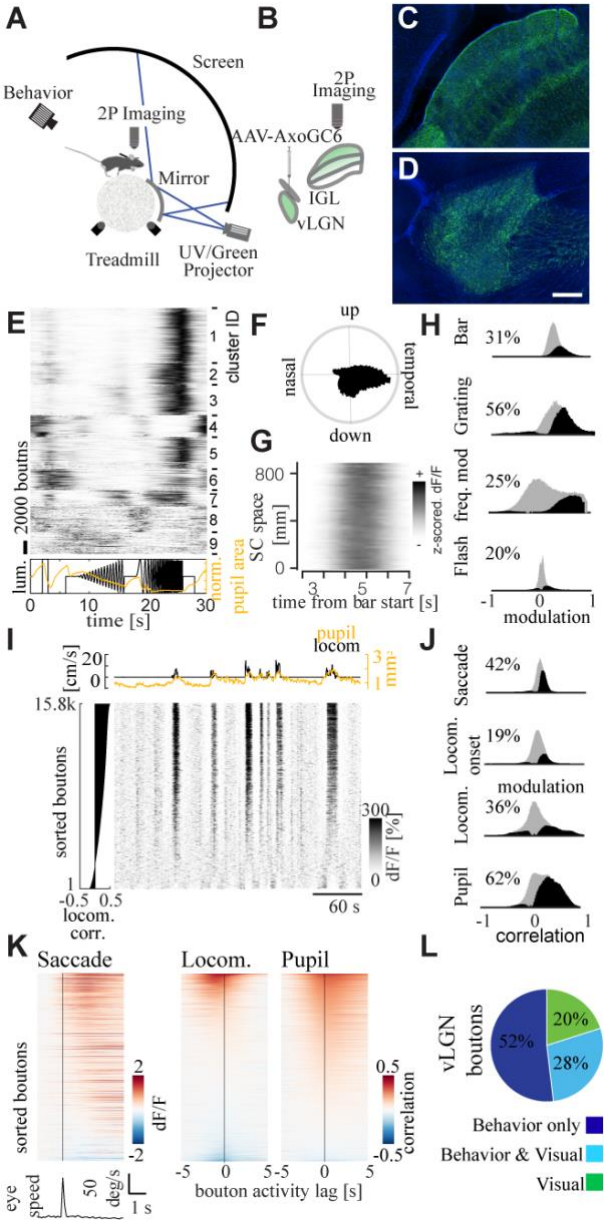

Fig. 3 vLGN/IGL terminals are strongly modulated by behavior. **A,** Schematic of the multi-photon imaging setup with mice head-fixed while running on a spherical treadmill and panoramic dome visual stimulation. **B**, Schematic of axon-GCaMP6s viral infection in Gad2^{+} neurons in the vLGN/IGL complex. **C,** Confocal image of the axonal termini in the sSC and (**D**) the infection area in the vLGN, sagittal view **E,** Cluster-sorted, averaged and z-scored responses (top) to full field luminance chirps (bottom, black line) of vLGN/IGL boutons (n = 220021, 38 recordings, 6 animals) in the sSC and average modulation of normalized pupil area (bottom, orange). **F,** Polar histogram of direction selective ($p < 0.01$, shuffle test) boutons' preferred direction in response to full field drifting gratings. **G,** z-scored and spatially binned (20 µm) bouton responses to moving bar across SC space. **H,** Histograms of modulation indices of vLGN/IGL bouton population (gray) and significantly modulated boutons (black & percentages) to visual stimuli. Two-sided Wilcoxon signed rank test, $p < 0.01$. **I,** Raster plot of example recording of vLGN/IGL boutons sorted by correlation with locomotion (left) and respective locomotion (black) and pupil area (orange, top) traces **J,** Histograms of modulation indices (saccades, locomotion onset) or correlation coefficients (locomotion speed, pupil area) of vLGN/IGL bouton population (gray) and significantly modulated boutons (black & percentages) to behavioral parameters. $p < 0.01$, two-sided Wilcoxon signed rank test, shuffle test for correlations (see methods) $p < 0.01$. **K,** Average modulation (saccade, bottom: average eye location speed) or cross-correlations (locomotion speed, pupil area) of vLGN/IGL bouton activity **L,** Pie chart of boutons

significantly modulated by any of the visual stimuli tested (**H**) and/or significantly modulated by/correlated to any of the behavioral parameters (**J**); $p < 0.01$, Bonferroni corrected for multiple comparisons. Scale bar: 100 µm.

vLGN/IGL complex activation drives actions.

Based on the strong inhibitory effect (Fig. 1) and visual modulation (Fig. 2), as well as the orchestrated behavioral activity conveyed by the vLGN/IGL complex (Fig. 3), this pathway acts as a feedback mechanism that could fine-tune visuomotor processes and adjust motor commands in real-time. Thus, we reasoned that the vLGN/IGL pathway, when optogenetically activated, should reveal motor command prediction errors related to those behaviors that were correlated with the measured activity at its terminals. To test this, we analyzed the behavioral responses to vLGN activation for the animals recorded previously (Fig. 2), focusing on locomotion, saccadic eye movements, and pupil size modulation (Fig. 4). Upon optogenetic activation (Fig. 4A), mice changed their walking direction and turned on the spherical treadmill strongly to the side of the optogenetic stimulation (Fig. 4B, Fig. S7A, B). We also observed robust gaze changes (Fig. 4C), which, on average, had a small corrective movement of ~3 ° and tended to increase in magnitude as the eye was moved away from the central position (Fig. 4D). Finally, we also observed a robust pupillary response with the pupil size increasing upon optogenetic stimulation independent of the initial dilation (Fig. 4E, F). All of these effects were absent during optogenetic stimulation in control animals (Fig. S7C-F). These results raise the question of whether vLGN stimulation motor effects are transmitted via the SC or other pathways. Although we cannot exclude the possibility that some of the information is transmitted via the SC, anatomical evidence suggests that the answer is more nuanced: vLGN projects to the pretectal olivary nucleus (Fig. S8A), an area known to directly activate the Edinger-Westphal nucleus, the strongest regulator of pupillary constriction (*39*). It also projects to the pons (Fig. S8B, C), and reticular gigantocellular nucleus (Gi) (Fig. S8D, E) and is involved in visuo-motor coordination and control of locomotion (*40*). Finally, we also observed direct projections to the paramedian pontine reticular formation (PMn) (Fig. S8D-F), an area suggested to be involved in eye movements (*41*). These results show that the vLGN/IGL complex orchestrate a visual and motor coordination.

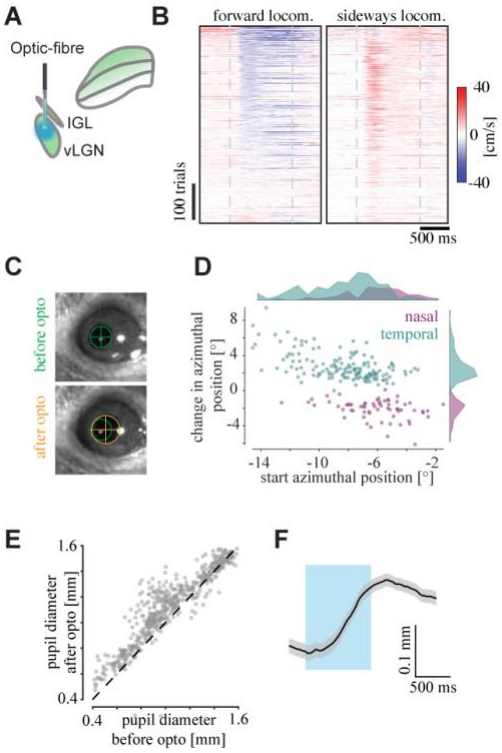

Fig. 4 vLGN/IGL complex modulates behavior. A, Schematic of viral Chr2 expression in Gad2$^+$ neurons in the vLGN/IGL complex. **B**, Optogenetically induced locomotion change for forward (left) and sideways (right) locomotion. Gray dashed lines represent the start and end of the optogenetic stimulation. **C**, Example images of an optogenetically induced saccade. Top, before optogenetic stimulation, bottom, after. Green and orange circles demarcate the size and position of the pupil, before and after stimulation, respectively. **D**, Magnitude and direction of optogenetically induced saccades (only saccades that exceeded a speed threshold were plotted - see methods). **E**, Optogenetically induced pupillary dilation. **F**, Average kinetics of optogenetically induced pupillary dilation.

vLGN refines percepts during voluntary movements.

Our physiological data (Fig. 1-3) and perturbation experiments (Fig. 4) suggest that the vLGN/IGL complex acts as a feedback regulator, anticipating the effects of movement on the animal's visual input. Thus, this pathway should be required to correct for movement related visual blurs, e.g., being involved in saccadic suppression, and for maintaining perceptual stability during behavior. We set out to test this hypothesis by chronically blocking bilateral vLGN output by expressing tetanus toxin light chain (TeLC) (*42*) in Gad2$^+$ vLGN/IGL neurons (Fig. 5A). First, we confirmed *in vitro* that TeLC blocks synaptic release (Fig. S9A-C). Next, we tested *in vivo* whether visual responses in SC were modified by flash and white noise stimulation (Fig. 5B top, Fig. S9). Neither the impulse responses nor the spatiotemporal filters showed any obvious difference, suggesting that feedforward visual processing is not affected. Similarly, pretectal visual behaviors, such as the optokinetic reflex, remained unaltered (Fig. 5C). Interestingly, we observed a reduction in the rate of pupil constriction to luminance changes (Fig. 5B, bottom, Fig. S9H-J), as well as a reduction in pupil dynamics during locomotion (Fig. 5D), supporting the notion that the vLGN fine-tunes visuomotor processes. We then hypothesized that the vLGN may be required to modulate visual responses during voluntary eye movements. To this end, we first compared bouton responses to saccades while displaying a stationary structured background with visually evoked responses to

"pseudosaccades" (movements of the displayed pattern that would mimic the visual input perceived during saccades, Fig. 5F-H) (*43*). As expected, retinal boutons in the SC responded similarly when the eye or visual stimulus moved (Fig. 5F). In contrast, vLGN boutons were mainly sensitive to real saccades (Fig. 5G), showing a clear preference for voluntary eye movement saccades over pseudosaccades (Fig. 5H). Similarly, at low contrast, vLGN boutons remained active while retinal processes reduced their visually evoked response during saccades (Fig. S10). Thus, blocking the vLGN with TeLC should alter the enhanced visual evoked responses driven by saccades. Indeed, when electrophysiologically recording SC neurons in animals in which the vLGN was blocked (Fig. 5I), we observed an increase in firing that prolonged the response by an average of 100 ms (Fig. 5J) and increased the average firing rate in the first 100 ms (Fig. 5K). These results suggest that these animals should have specific perceptual deficits in interpreting visual signals during motion.

Recently, it has been shown that mice can use monocular and binocular cues to estimate depth (*44*) and that monocular perception requires motion for proper depth estimation (*45*). Therefore, we decided to test depth perception using a classical visual cliff paradigm (Fig. 5L, top), which has been shown to be monocular (*44*). For these experiments, we clipped the whiskers to minimize tactile sensory input, placed the animals on the platform, and recorded their behavior. Control mice showed a strong preference for the platform, but also roamed around the edges of the arena, possibly by touching the walls with their bodies (Fig. 5M, top). We therefore excluded these events from our analysis. When comparing preference in vLGN-blocked mice, we saw a strong reduction in cliff avoidance (Fig. 5M, N). Next, we tested whether mice preferred to exit either near the walls or toward the center of the platform. While both control and vLGN/IGL-blocked animals exited the platform toward the cliff, vLGN-blocked mice showed a trend of increased exit events toward the center of the platform (Fig. 5O, P). When quantifying the number of times that mice stopped in front of the cliff and aborted the exit movement, vLGN-blocked animals showed a large reduction compared to control animals (Fig. 5Q, R), indicating that they may have difficulty judging depth. Taken together, these results show that visuomotor processing and perception during self-generated motion are impaired in the absence of proper vLGN/IGL function.

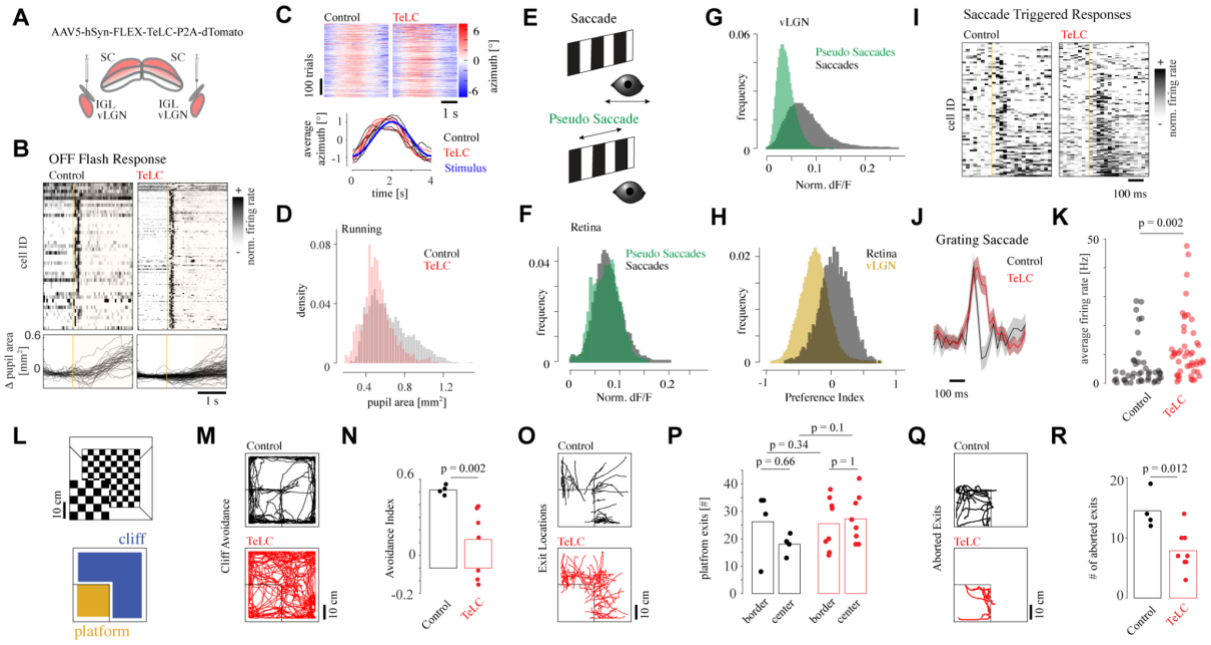

Fig. 5 vLGN/IGL activity is required for visuomotor transformations and proper visual perception. A, Brain schematic showing the location of the viral injections for TeLC expression in Gad2-cre mice. **B**, Average visual responses to full-field flashes in control and TeLC-expressing mice (top) and corresponding pupil size changes (bottom). **C**, Example of optokinetic reflex responses to sinusoidal moving checkerboard stimuli (top) and average per animal (bottom). **D**, Quantization of the pupil size distributions during locomotion in control and TeLC animals. **E,** Spontaneous saccades on a stationary grating or checkerboard ("saccades", top, black) and saccade-like shifts of the displayed texture during stationary eye periods ("pseudosaccades", bottom, green) induce comparable image shifts. **F**, Normalized responses is retinal boutons ($p < 0.0001$, effect size $r = 0.1$, paired, two-tailed Wilcoxon signed-rank test, $n = 517$ to the stimuli in (**E**). **G**, vLGN boutons are mainly driven by saccadic motion ($p < 0.0001$, effect size $r = -0.34$, $n = 51996$). **H**, Histograms of the bouton-wise pseudosaccade preference index for RGC (gray) and vLGN (yellow) bouton responses as in (**F, G**) with a preference for vLGN boutons shifted to the negative compared to RGC ($p < 0.0001$, two-tailed Wilcoxon rank sum test). **I**, Normalized PSTH of mean saccade-triggering responses in control (left) and TeLC (right) mice. **J**, Normalized population-averaged saccade responses and SEM (shading) and (**K**) average firing rate for the first 100 ms after saccade onset. **L**, Schematic of the visual cliff setup (top) and areas used for subsequent quantification (bottom). **M**, Examples of running trajectories during the first 15 min for control and TeLC mice and (**N**) quantification per animal (Wilcoxon rank sum test). **O**, Same as (**M**) but showing only trajectories for platform exits (1 s before and after crossing). (**P**) Quantification of exits clustered on position (Wilcoxon rank sum test). **Q**, as (**M**), but only showing trajectories for aborted exits (2 s before and after a detected crossing with the subsequent reversal of the motion velocity, see Methods) and (**R**) the corresponding quantification (Wilcoxon rank sum test).

Discussion

All animals require mechanisms to distinguish sensory inputs caused by their own movements (reafferent) from sensory inputs caused by sources in the outside world (exafferent) (Fig. 1A). In the visual system, several mechanisms have been proposed to support such perceptual tasks. These start at the retina, where retinal ganglion cells have been described to subtract object motion from background motion (*46*). Similarly, other retinal mechanisms have been proposed to suppress visual responses generated by saccadic eye movements (*47*). These retinal processes act in concert with ocular stabilization mechanisms such as the vestibulo-ocular reflex (VOR) (*48*). In rodents, the VOR stabilizes the eye, and thus the retinal image,

remarkably well during head movements, on average by ~10° in visual angle (*49*, *50*), and supports visual pursuit behavior by stabilizing prey in binocular retinal regions (*51*). However, despite this precisely tuned motor feedback system, there are several types of self-induced visual motion that cannot be stabilized, e.g., visual motion during translational movements. An additional strategy for providing corrective signals is via corollary discharges (CD) (*1*), neural mechanisms that involve the transmission of a copy of motor commands or signals from a brain region involved in generating motor output to brain regions processing sensory information. Thus, a CD can provide a predictive signal about the expected sensory feedback resulting from the motor command. In the visual system, CD has been extensively studied in the context of saccades, rapid eye movements that would temporarily blur visual perception. To minimize this perceptual blurring, a process called saccadic suppression has been found across species (*52–57*). Most notably, it has been studied in primates, where ascending pathways run from the midbrain (*6*) to the frontal eye field, a cortical structure involved in visual processing and oculomotor control (*58*).

Beyond saccadic eye movements, reafference signals induced by self-motion will affect visual processing in a variety of ways. One approach would be for several different brain areas to act sequentially to generate CDs to compensate for different behaviors. However, it is challenging to maintain a reliable sensory representation through sequential filtering steps. An alternative approach would be to pool all possible behavioral signals at a CD hub and modulate sensory signals according to the best overall estimate of the currently executed movement ensemble, ideally at the first possible step. Here, we provide evidence for the latter by showing that a strong inhibitory projection from the vLGN/IGL complex (Fig. 1) modulates visual signals in the superficial superior colliculus (Fig. 2). We found that this inhibitory projection mediates a combination of visual and behavioral parameters (Fig. 3) that are distinct from direct visual inputs from the retina (Fig. S5). In comparison, while retinal terminals show a variety of visual responses as previously shown (*35*), vLGN terminals are mainly driven by high-frequency luminance modulation and front-to-back visual motion (Fig. 3), stimuli that occur during forward locomotion in natural environments. Actions, such as saccades, locomotion, or pupillary dilation during minimal visual interest, barely modulate retinal inputs but strongly drive the vLGN projection. In addition, vLGN activity increases before or in synchrony with behavior, coinciding with the arrival of visual inputs from the retina. (Fig. S6E-G). Taken together, these results support the hypothesis that the vLGN/IGL complex acts as a corollary discharge hub integrating diverse behavioral and visual information elicited during behavior to modulate visual information in the midbrain.

The role of CDs is to regulate sensory signals, allowing the brain to compare predicted sensory inputs that originate through behavior with actual sensory signals. Such a feedback loop would enable constant adjustments of visuomotor transformations in real time (*1*, *6*), and thus improve perception. From this perspective, targeted activation of CDs should reveal corrective movements that may qualitatively overlap with the neural signals they convey (Fig. 3). Indeed, this is exactly what we observed. Optogenetic activation of the vLGN triggers changes in locomotor speed, saccadic eye movements and changes in pupil size (Fig. 4), suggesting a more

active role for the vLGN/IGL complex in fine-tuning visuomotor transformations. Interestingly, these motor commands not necessarily exert their influence through the visual pathway in the SC, but directly through other subcortical target areas known to strongly influence these behaviors, such as Gi (*40*), paramedian reticular nucleus (*41*), and Edinger-Westphal nucleus via the olivary pretectal nucleus (*39*) (Fig. S7). Consistent with these results, blocking vLGN output alters the dynamics of pupil construction and visual signal processing during saccades (Fig. 5).

While we investigated vLGN's function mostly in situations where visual and behavioral signals were intentionally separated, during natural behavior movement-induced reafferent and exafferent signals are strongly and necessarily intermixed, as during saccades. These signals need to be discriminated, e.g., to estimate distance using monocular cues (*44*, *45*). Accordingly, using the visual cliff paradigm, we were able to show that vLGN-deficient mice have severe impairments in depth perception (Fig. 5).

In conclusion, the vLGN/IGL complex plays a fundamental role in the coordination of motor actions and visual processing, thereby maintaining perceptual stability. Our results underscore how closely vision and motion are linked to enable effective interaction with the sensory environment.

References and Notes

1. T. B. Crapse, M. A. Sommer, Corollary discharge across the animal kingdom. *Nat. Rev. Neurosci.* **9**, 587–600 (2008).

2. J. J. Gibson, Visually controlled locomotion and visual orientation in animals. *Br. J. Psychol.* **49**, 182–194 (1958).

3. K. E. Cullen, The vestibular system: multimodal integration and encoding of self-motion for motor control. *Trends Neurosci.* **35**, 185–196 (2012).

4. D. McNamee, D. M. Wolpert, Internal Models in Biological Control. *Annu Rev Control Robot Auton Syst.* **2**, 339–364 (2019).

5. R. H. Wurtz, Corollary Discharge Contributions to Perceptual Continuity Across Saccades. *Annu Rev Vis Sci*. **4**, 215–237 (2018).

6. M. A. Sommer, R. H. Wurtz, Brain circuits for the internal monitoring of movements. *Annu. Rev. Neurosci.* **31**, 317–338 (2008).

7. T. Isa, E. Marquez-Legorreta, S. Grillner, E. K. Scott, The tectum/superior colliculus as the vertebrate solution for spatial sensory integration and action. *Curr. Biol.* **31**, R741–R762 (2021).

8. C. Massot, U. K. Jagadisan, N. J. Gandhi, Sensorimotor transformation elicits systematic patterns of activity along the dorsoventral extent of the superior colliculus in the macaque monkey. *Commun Biol*. **2**, 287 (2019).

9. N. J. Gandhi, H. A. Katnani, Motor functions of the superior colliculus. *Annu. Rev. Neurosci.* **34**, 205–231 (2011).

10. R. J. Krauzlis, L. P. Lovejoy, A. Zénon, Superior colliculus and visual spatial attention. *Annu. Rev. Neurosci.* **36**, 165–182 (2013).

11. M. A. Basso, M. E. Bickford, J. Cang, Unraveling circuits of visual perception and cognition through the superior colliculus. *Neuron*. **109**, 918–937 (2021).

12. B. de Gelder, M. Tamietto, G. van Boxtel, R. Goebel, A. Sahraie, J. van den Stock, B. M. C. Stienen, L. Weiskrantz, A. Pegna, Intact navigation skills after bilateral loss of striate cortex. *Curr. Biol.* **18**, R1128-9 (2008).

13. X. Zhao, M. Liu, J. Cang, Visual cortex modulates the magnitude but not the selectivity of looming-evoked responses in the superior colliculus of awake mice. *Neuron*. **84**, 202–213 (2014).

14. H. Straka, J. Simmers, B. P. Chagnaud, A New Perspective on Predictive Motor Signaling. *Curr. Biol.* **28**, R232–R243 (2018).

15. L. D. Salay, A. D. Huberman, Divergent outputs of the ventral lateral geniculate nucleus mediate visually evoked defensive behaviors. *Cell Rep.* **37**, 109792 (2021).

16. A. Fratzl, A. M. Koltchev, N. Vissers, Y. L. Tan, A. Marques-Smith, A. V. Stempel, T. Branco, S. B. Hofer, Flexible inhibitory control of visually evoked defensive behavior by the ventral lateral geniculate nucleus. *Neuron*. **109**, 3810-3822.e9 (2021).

17. C. Shang, A. Liu, D. Li, Z. Xie, Z. Chen, M. Huang, Y. Li, Y. Wang, W. L. Shen, P. Cao, A subcortical excitatory circuit for sensory-triggered predatory hunting in mice. *Nat. Neurosci.* **22**, 909–920 (2019).

18. K. Kaneda, K. Isa, Y. Yanagawa, T. Isa, Nigral inhibition of GABAergic neurons in mouse superior colliculus. *J. Neurosci.* **28**, 11071–11078 (2008).

19. M. Conley, B. Friederich-Ecsy, Functional organization of the ventral lateral geniculate complex of the tree shrew (Tupaia belangeri): I. Nuclear subdivisions and retinal projections. *J. Comp. Neurol.* **328**, 1–20 (1993).

20. M. E. Harrington, The ventral lateral geniculate nucleus and the intergeniculate leaflet: interrelated structures in the visual and circadian systems. *Neurosci. Biobehav. Rev.* **21**, 705–727 (1997).

21. S. Pateromichelakis, Response properties of units in the lateral geniculate nucleus of the domestic chick (Gallus domesticus). *Brain Res.* **167**, 281–296 (1979).

22. Z. Hu, Y. Mu, L. Huang, Y. Hu, Z. Chen, Y. Yang, X. Huang, Y. Fu, Y. Xi, S. Lin, Q. Tao, F. Xu, K.-F. So, C. Ren, A visual circuit related to the periaqueductal gray area for the antinociceptive effects of bright light treatment. *Neuron*. **110**, 1712-1727.e7 (2022).

23. H. R. Maturana, F. J. Varela, Color-opponent responses in the avian lateral geniculate: a study in the quail (Coturnix coturnix japonica). *Brain Res.* **247**, 227–241 (1982).

24. H. Gioanni, A. Palacios, A. Sansonetti, F. Varela, Role of the nucleus geniculatus lateralis ventralis (GLv) in the optokinetic reflex: a lesion study in the pigeon. *Exp. Brain Res.* **86**, 601–607 (1991).

25. G. D. Guiloff, H. R. Maturana, F. J. Varela, Cytoarchitecture of the avian ventral lateral geniculate nucleus. *J. Comp. Neurol.* **264**, 509–526 (1987).

26. T. Vega-Zuniga, J. Mpodozis, H. J. Karten, G. Marín, S. Hain, H. Luksch, Morphology, projection pattern, and neurochemical identity of Cajal's "centrifugal neurons": the cells of

origin of the tectoventrogeniculate pathway in pigeon (Columba livia) and chicken (Gallus gallus). *J. Comp. Neurol.* **522**, 2377–2396 (2014).

27. T. Vega-Zuniga, G. Marín, C. González-Cabrera, E. Planitscher, A. Hartmann, V. Marks, J. Mpodozis, H. Luksch, Microconnectomics of the pretectum and ventral thalamus in the chicken (Gallus gallus). *J. Comp. Neurol.* **524**, 2208–2229 (2016).

28. T. Vega-Zuniga, D. Trost, K. Schicker, E. M. Bogner, H. Luksch, The Medial Ventrothalamic Circuitry: Cells Implicated in a Bimodal Network. *Front. Neural Circuits*. **12**, 9 (2018).

29. S. D. Gale, G. J. Murphy, Distinct representation and distribution of visual information by specific cell types in mouse superficial superior colliculus. *J. Neurosci.* **34**, 13458–13471 (2014).

30. A. Monavarfeshani, U. Sabbagh, M. A. Fox, Not a one-trick pony: Diverse connectivity and functions of the rodent lateral geniculate complex. *Vis. Neurosci.* **34**, E012 (2017).

31. A. Sumser, M. Joesch, P. Jonas, Y. Ben-Simon, Fast, high-throughput production of improved rabies viral vectors for specific, efficient and versatile transsynaptic retrograde labeling. *Elife*. **11** (2022), doi:10.7554/eLife.79848.

32. Z. Li, B. Peng, J. J. Huang, Y. Zhang, M. B. Seo, Q. Fang, G.-W. Zhang, X. Zhang, L. I. Zhang, H. W. Tao, Enhancement and contextual modulation of visuospatial processing by thalamocollicular projections from ventral lateral geniculate nucleus. *Nat. Commun.* **14**, 7278 (2023).

33. T. Gollisch, M. Meister, Rapid neural coding in the retina with relative spike latencies. *Science*. **319**, 1108–1111 (2008).

34. Y. Zhang, M. Rózsa, Y. Liang, D. Bushey, Z. Wei, J. Zheng, D. Reep, G. J. Broussard, A. Tsang, G. Tsegaye, S. Narayan, C. J. Obara, J.-X. Lim, R. Patel, R. Zhang, M. B. Ahrens, G. C. Turner, S. S.-H. Wang, W. L. Korff, E. R. Schreiter, K. Svoboda, J. P. Hasseman, I. Kolb, L. L. Looger, Fast and sensitive GCaMP calcium indicators for imaging neural populations. *bioRxiv* (2021), , doi:10.1101/2021.11.08.467793.

35. T. Baden, P. Berens, K. Franke, M. Román Rosón, M. Bethge, T. Euler, The functional diversity of retinal ganglion cells in the mouse. *Nature*. **529**, 345–350 (2016).

36. U. M. Ciftcioglu, V. Suresh, K. R. Ding, F. T. Sommer, J. A. Hirsch, Visual Information Processing in the Ventral Division of the Mouse Lateral Geniculate Nucleus of the Thalamus. *J. Neurosci.* **40**, 5019–5032 (2020).

37. D. Gupta, W. Młynarski, A. Sumser, O. Symonova, J. Svatoň, M. Joesch, Panoramic visual statistics shape retina-wide organization of receptive fields. *Nat. Neurosci.* **26**, 606–614 (2023).

38. S. Schröder, N. A. Steinmetz, M. Krumin, M. Pachitariu, M. Rizzi, L. Lagnado, K. D. Harris, M. Carandini, Arousal Modulates Retinal Output. *Neuron*. **107**, 487-495.e9 (2020).

39. D. H. McDougal, P. D. Gamlin, Autonomic control of the eye. *Compr. Physiol.* **5**, 439–473 (2015).

40. M. Lemieux, F. Bretzner, Glutamatergic neurons of the gigantocellular reticular nucleus shape locomotor pattern and rhythm in the freely behaving mouse. *PLoS Biol.* **17**, e2003880 (2019).

41. B. Cohen, V. Henn, Unit activity in the pontine reticular formation associated with eye

movements. *Brain Res.* **46**, 403–410 (1972).

42. S. L. Pashkovski, G. Iurilli, D. Brann, D. Chicharro, K. Drummey, K. M. Franks, S. Panzeri, S. R. Datta, Structure and flexibility in cortical representations of odour space. *Nature*. **583**, 253–258 (2020).

43. S. K. Miura, M. Scanziani, Distinguishing externally from saccade-induced motion in visual cortex. *Nature*. **610**, 135–142 (2022).

44. H. C. Boone, J. M. Samonds, E. C. Crouse, C. Barr, N. J. Priebe, A. W. McGee, Natural binocular depth discrimination behavior in mice explained by visual cortical activity. *Curr. Biol.* **31**, 2191-2198.e3 (2021).

45. P. R. L. Parker, E. T. T. Abe, N. T. Beatie, E. S. P. Leonard, D. M. Martins, S. L. Sharp, D. G. Wyrick, L. Mazzucato, C. M. Niell, Distance estimation from monocular cues in an ethological visuomotor task. *Elife*. **11** (2022), doi:10.7554/eLife.74708.

46. B. P. Olveczky, S. A. Baccus, M. Meister, Segregation of object and background motion in the retina. *Nature*. **423**, 401–408 (2003).

47. S. Idrees, M. P. Baumann, F. Franke, T. A. Münch, Z. M. Hafed, Perceptual saccadic suppression starts in the retina. *Nat. Commun.* **11**, 1977 (2020).

48. M. Ito, Cerebellar control of the vestibulo-ocular reflex--around the flocculus hypothesis. *Annu. Rev. Neurosci.* **5**, 275–296 (1982).

49. A. F. Meyer, J. O'Keefe, J. Poort, Two distinct types of eye-head coupling in freely moving mice. *Curr. Biol.* **30**, 2116-2130.e6 (2020).

50. D. J. Wallace, D. S. Greenberg, J. Sawinski, S. Rulla, G. Notaro, J. N. D. Kerr, Rats maintain an overhead binocular field at the expense of constant fusion. *Nature*. **498**, 65–69 (2013).

51. C. D. Holmgren, P. Stahr, D. J. Wallace, K.-M. Voit, E. J. Matheson, J. Sawinski, G. Bassetto, J. N. Kerr, Visual pursuit behavior in mice maintains the pursued prey on the retinal region with least optic flow. *Elife*. **10** (2021), doi:10.7554/eLife.70838.

52. J. Ross, M. C. Morrone, M. E. Goldberg, D. C. Burr, Changes in visual perception at the time of saccades. *Trends Neurosci.* **24**, 113–121 (2001).

53. M. Zaretsky, C. H. Rowell, Saccadic suppression by corollary discharge in the locust. *Nature*. **280**, 583–585 (1979).

54. A. Thiele, P. Henning, M. Kubischik, K.-P. Hoffmann, Neural mechanisms of saccadic suppression. *Science*. **295**, 2460–2462 (2002).

55. D. Lee, J. G. Malpeli, Effects of saccades on the activity of neurons in the cat lateral geniculate nucleus. *J. Neurophysiol.* **79**, 922–936 (1998).

56. A. J. Kim, L. M. Fenk, C. Lyu, G. Maimon, Quantitative Predictions Orchestrate Visual Signaling in Drosophila. *Cell*. **168**, 280-294.e12 (2017).

57. M. A. Ali, K. Lischka, S. J. Preuss, C. A. Trivedi, J. H. Bollmann, A synaptic corollary discharge signal suppresses midbrain visual processing during saccade-like locomotion. *Nat. Commun.* **14**, 7592 (2023).

58. J. D. Schall, On the role of frontal eye field in guiding attention and saccades. *Vision Res.* **44**,

1453–1467 (2004).

59. M. Pachitariu, N. Steinmetz, S. Kadir, M. Carandini, K. D. Harris, Kilosort: realtime spike-sorting for extracellular electrophysiology with hundreds of channels. *bioRxiv* (2016), p. 061481.

60. A. Mathis, P. Mamidanna, K. M. Cury, T. Abe, V. N. Murthy, M. W. Mathis, M. Bethge, DeepLabCut: markerless pose estimation of user-defined body parts with deep learning. *Nat. Neurosci.* **21**, 1281–1289 (2018).

61. D. H. Brainard, The Psychophysics Toolbox. *Spat. Vis.* **10**, 433–436 (1997).

62. W. Aziz, W. Wang, S. Kesaf, A. A. Mohamed, Y. Fukazawa, R. Shigemoto, Distinct kinetics of synaptic structural plasticity, memory formation, and memory decay in massed and spaced learning. *Proc. Natl. Acad. Sci. U. S. A.* **111**, E194-202 (2014).

63. K. H. Lee, A. Tran, Z. Turan, M. Meister, The sifting of visual information in the superior colliculus. *Elife*. **9** (2020), doi:10.7554/eLife.50678.

64. I. Stitt, E. Galindo-Leon, F. Pieper, G. Engler, A. K. Engel, Laminar profile of visual response properties in ferret superior colliculus. *J. Neurophysiol.* **110**, 1333–1345 (2013).

65. J. S. Montijn, K. Seignette, M. H. Howlett, J. L. Cazemier, M. Kamermans, C. N. Levelt, J. A. Heimel, A parameter-free statistical test for neuronal responsiveness. *Elife*. **10** (2021), doi:10.7554/eLife.71969.

66. Introduction to the practice of statistics. *Technometrics*. **46**, 118–119 (2004).

67. T. M. Ryan, A. J. Hinojosa, R. Vroman, C. Papasavvas, L. Lagnado, Correction of z-motion artefacts to allow population imaging of synaptic activity in behaving mice. *J. Physiol.* **598**, 1809–1827 (2020).

68. M. Pachitariu, C. Stringer, M. Dipoppa, S. Schröder, L. Federico Rossi, H. Dalgleish, M. Carandini, K. D. Harris, Suite2p: beyond 10,000 neurons with standard two-photon microscopy. *bioRxiv* (2017), p. 061507.

69. G. B. Keller, T. Bonhoeffer, M. Hübener, Sensorimotor Mismatch Signals in Primary Visual Cortex of the Behaving Mouse. *Neuron*. **74** (2012), pp. 809–815.

70. D. A. Dombeck, A. N. Khabbaz, F. Collman, T. L. Adelman, D. W. Tank, Imaging large-scale neural activity with cellular resolution in awake, mobile mice. *Neuron*. **56**, 43–57 (2007).

Acknowledgments: We thank Yoav Ben Simon for generously making viral vectors for retrograde tracing available. We also thank Wiktor Młynarski and members of the Neuroethology group for their comments on the manuscript. This research was supported by the Scientific Service Units of IST Austria through resources provided by Scientific Computing, the Preclinical Facility, the Lab Support Facility, and the Imaging and Optics Facility, in particular Freyja Lange, Michael Schunn and Todor Asenov.

Funding:

EMBO ALTF 1098-2017 (AS)

Human Frontiers Science Program LT000256/2018-L (AS)

European Research Council Starting Grant 756502 (MJ).

Author contributions:
Conceptualization: TVZ, AS, MJ
Investigation: TVZ, AS, PK, FS
Methodology: TVZ, AS, PK, OS
Software: AS, OS
Visualization: TVZ, AS, OS, MJ
Resources: MJ
Funding acquisition: AS, MJ
Writing – original draft: MJ
Writing – review & editing: TVZ, AS, PK, FS, OS, MJ

Competing interests: Authors declare that they have no competing interests.

Data and materials availability: All data as well as analysis code used in the work will be available at ISTA DataRep and Github upon publication.

Material and Methods

Statistics and Reproducibility

No statistical method was used to predetermine sample size. Extracellularly recorded units and imaged bouton ROIs were selected excluded based on quality and response criteria as described below.

Animals

Animal protocols were reviewed by the institutional preclinical core facility at IST Austria. All breeding and experimentation were performed under a license approved by the Austrian Federal Ministry of Science and Research in accordance with the Austrian and EU animal laws (BMF-66.018/0017-WF/V/3b/2017). During the experimental phase, mice were housed individually in standard macrolon cages with red plastic houses, running wheels and enrichment consisting of wood chips and nesting material at an inverted 12-hour light cycle. Experiments were done during the dark phase of the light cycle.

For *in vivo* tracing experiments, *ex vivo* patch-clamp experiments, *in vivo* opto/electrophysiology and *in vivo* TeLC experiments, Gad2-IRES-Cre (JAX, #010802; n = 10, 6 males, 4 females; n = 8, 5 males, 3 females; 6, 4 males, 2 females; n = 12, 6 males, 6 females, respectively), aged 8 weeks at viral injection were used, respectively.

For *in vivo* anterograde transsynaptic experiments, Ai75D (JAX, # 025106, n = 6, 4 males, 2 females), aged 8 weeks at viral injection were used. For *in vivo* retrograde transsynaptic experiments, NTSR1-GN209-Cre (MMRRC, #030780, n = 4, 2 males, 2 females), GRP-KH288-cre (MMRRC, #031183, n = 4, 2 males, 2 females), and Rorb-Cre (JAX, # 023526, n = 4, 2 males, 2 females), aged 8 weeks at viral injection were used. For *in vivo* vLGN terminal imaging experiments, Gad2-IRES-Cre (JAX, #010802; n = 6, 4 males, 2 females), aged 5–12 weeks at viral infection and implantation were used. The mice for retinal terminal imaging experiments were C57BL/6J (JAX, #000664; n = 5, 3 males, 2 females), aged 6–11 weeks at eye injection. Of those, 3 mice have been used to record previously published separate datasets (*37*).

Viral vectors

Calcium indicator expression in vLGN/IGL neurons was achieved with AAV-hSynapsin1-FLEx-axon-GCaMP6s (1×10^{12} genome copies per ml, Addgene, 112010-AAV5) for retinal expression AAV2.7M8-syn-GCaMP8m viral vectors (1×10^{13} genome copies per ml), generated at ISTA viral facility. Tetanus Neurotoxin Light Chain (TeLC) viruses were generated using AAV5-hSyn-FLEX-TeLC-P2A-dTomato (Addgene, 159102, 1×10^{13} genome copies per ml) at ISTA viral facility. ChR2 (AAV5-EF1a-doubleFloxed-hChR2(H134R)-EYFP-WPRE-HGHpa (#20298-AAV5), 1×10^{13} genome copies per ml) and mCherry control (AAV5-hSyn-DIO-mCherry (#50459-AAV5), 7×10^{12} genome copies per ml) viruses were purchased from Addgene.

Anterograde transsynaptic expression was done with AAV1-cre (AAV1.CamKII0.4.Cre.SV40, 7×10^{12} vg/mL, Addgene). Retrograde transsynaptic expression was performed with starter

vector (AAV-DIO-Ef1a-TVA-FLAG-2A-N2C_G) (*31*) and pseudotyped rabies vector (N2C(Enva)-EGFP, ~2–5 x10^8 TU ml^{-1}) (*31*).

Stereotaxic viral injections

Mice were induced with 3 % isoflurane and anesthetized with intraperitoneal (i.p.) ketaminexylazine (100 mg kg^{-1}, 10 mg kg^{-1}). As an analgesic, meloxicam (20 mg kg^{-1}) was subcutaneously injected. Mice were placed in a stereotaxic apparatus (Kopf) and body temperature was controlled with a heating pad at 37 °C throughout the whole procedure. Stereotaxic target coordinates relative to bregma were -2.3 mm (AP), 2.4 mm (ML), 3.4 mm (DV) for vLGN, -3.8 mm (AP), 0.8 mm (ML), 1.3 mm (DV) for SC and 4 mm (AP), 2.6 mm (2.6 mm (ML), 0.5 mm (DV) for visual cortex injection. Glass electrodes were pulled with a one-stage puller (DMZ-Zeitz-Puller) to produce a tip opening ~30 µm. The pipette was filled with mineral oil, then attached to a Nanoliter 2010 (World Precision Instruments) and loaded with the respective vector. Pipettes were slowly lowered to the target region (vLGN and SC 300 nl, V1 60 nL) of the solution was injected at a rate of 45 nl min^{-1}. Once the volume was delivered, pipettes remained in place for 15 min before being carefully withdrawn and the incision closed with VetBond (3M). For vLGN terminal imaging experiments, in 4 out of 6 mice, viral infection was immediately followed by cranial window implantation in the same surgery. The remaining 2 mice were implanted 4 weeks after the injection surgery.

***In vitro* electrophysiology**

Mice were deeply anesthetized via intraperitoneal (i.p.) injection of ketamine (95 mg kg^{-1}) and xylazine (4.5 mg kg^{-1}), followed by transcardial perfusion with ice-cold, oxygenated (95 % O_2, 5 % CO_2) artificial cerebrospinal fluid (ACSF) containing (in mM): 118 NaCl, 2.5 KCl, 1.25 NaH_2PO_4, 1.5 $MgSO_4$, 1 $CaCl_2$, 10 Glucose, 3 Myo-inositol, 30 Sucrose, 30 $NaHCO_3$; pH = 7.4. The brain was rapidly excised and coronal sections of 300 µm thickness containing the SC were cut using a Linear-Pro7 vibratome (Dosaka, Japan). Slices were left to recover for 20 min at 35 °C, followed by a slow cool down to room temperature (RT) over 40 – 60 min. After recovery, one slice was transferred to the recording chamber (RC-26GLP, Warner Instruments, Holliston, MA, USA) and superfused with ACSF containing 2 mM $CaCl_2$ at a rate of 3 – 4 ml/min at RT (21.0 - 23.0 °C). Glass pipettes (B150-86-10, Sutter Instrument, Novato, CA, USA) with resistances of 3 – 4 MΩ were crafted using a P1000 horizontal pipette puller (Sutter Instrument) and filled with internal solution containing (in mM): 140 K-Gluconate, 2 $MgCl_2$, 2 MgATP, 0.2 NaGTP, 0.5 EGTA, 10 HEPES; pH 7.4 adjusted with KOH. Biocytin (0.2 – 0.3 %) was added to the internal solution for post hoc morphological reconstruction. Electrical signals were acquired at 20 – 50 kHz and filtered at 4 kHz using a Multiclamp 700B amplifier (Molecular Devices, San Jose, CA, USA) connected to a Digidata 1440A digitizer (Molecular Devices) with pClamp10 software (Molecular Devices). For optogenetically evoked inhibitory postsynaptic currents (IPSCs), neurons were held at -60 mV and blue light (λ = 465 nm, 10 – 20 mW/cm^2 intensity, 5 ms pulse duration, 0.1 - 0.2 Hz stimulation frequency) was emitted through a mono fiber-optic cannula (5 mm length, fiber diameter 200 µm, total diameter 230 µm, Doric lenses, Quebec, Canada) connected to a PlexBright LED 644 (Plexon, Dallas, TX,

USA) with an optical patch cable (fiber diameter 200 µm, total diameter 230 µm, 0.48 NA). To block $GABA_A$ receptors, ACSF containing 20 µM bicuculline was bath-applied for 20-30 s followed by immediate washout. Access resistance was constantly monitored between protocols and recordings with access resistances exceeding 20 MΩ or with changes in access resistance or holding current by more than 20 % were discarded. After recordings, the pipette was carefully withdrawn and the slice was transferred to 4 % paraformaldehyde (PFA) in PBS solution.

Viral eye injections

For expression of calcium indicators in retinal neurons, C57BL/6J mice were anesthetized with ketamine/xylazine by i.p. injection. A small hole in the temporal eye, below the cornea, was cut with a 1/2-inch, 30-gauge needle. Subsequently, 1 µl of vitreous fluid was withdrawn and 1 µl of AAV2.7M8-syn-GCaMP8m viral vector solution was injected into the subretinal space with a Hamilton syringe and a 33-gauge blunt-ended needle. Mice were left to recover and viral expression was to commence for 2-4 weeks before implantation of the cranial window.

Cranial window implantation surgery

Cranial window implantation was performed as described previously (*37*). In brief, mice were injected with meloxicam (20 mg per kg body weight, subcutaneous (s.c.), 3.125 mg ml^{-1} solution) and dexamethasone (0.2 mg per kg body weight i.p., 0.02 mg ml^{-1} solution). Anesthesia was induced by 2.5 % isoflurane in oxygen in an anesthesia chamber and maintained at 0.7 % to 1.2 % in a stereotaxic device (Kopf), while body temperature was controlled by a heating pad to 37.5 °C. After exposing and cleaning the cranium, a 4 mm circular craniotomy was drilled above the left SC, the dura mater was removed, the left transverse sinus was sutured twice with 9-0 monofil surgical suture material (B. Braun) and cut between the sutures. Cortical areas covering the left SC were aspirated with a cell culture vacuum pump (Accuris), and a 3 mm circular coverslip, glued (Norland optical adhesives 61) to a stainless-steel conical ring, was inserted with the glass flush on the surface of the SC. After filling the surrounding cavity with Dura-Gel (Cambridge Neurotech) the insert was fixed in place with VetBond (3M). Finally, a custom-designed $TiAl_6V_4$ head-plate was affixed to the cranium by sequential application and curing of (1) All-in-One Optibond (Kerr), (2) Charisma Flow (Kulzer), and (3) Paladur (Kulzer). Mice were given 300 µl of saline and 20 mg per kg body weight meloxicam (s.c.) before removing them from the stereotaxic frame and letting them wake up while keeping them warm on a heating pad. Another dose of 20 mg per kg body weight meloxicam s.c. and 0.2 mg per kg body weight i.p. dexamethasone was further injected 24 h after the conclusion of the surgery. After the implantation surgery, mice were allowed to recover for at least one week.

In vivo electrophysiology and optogenetics

Gad2-Cre mice injected with AAV5-EF1a-doubleFloxed-hChR2(H134R)-EYFP were anesthetized and placed in the stereotaxic apparatus. The skull was exposed and the periosteum and connective tissue were removed. Thin crossed grooves over the bone were cut to increase the contact surface using a scalpel. The skull was covered with a thin layer of cyanoacrylate that was blue-light-cured for 45 s (VetBond; WPI). A second layer of Charisma was added and cured before securing the head plate with Super-Bond dental adhesive resin cement (Sun medical). A tapered Optic **λ**-fiber with an active zone of 0.5 mm (NA 0.39, Optogenix) was implanted using the same vLGN coordinates and craniotomy. **λ**-fibers have the advantage of having a sharp tip, disrupting less tissue during penetration and emitting diffusely from the taper. The tip of the fiber was slowly lowered to a depth of 3.4 mm from the dorsal surface and cemented to the skull. One day prior to the recording session, mice were anesthetized with isoflurane (1 % - 1.5 % in oxygen 0.8 l min^{-1}) and meloxicam (20 mg kg^{-1}) were injected subcutaneously as an analgesic. A small craniotomy was made in the rostral skull (Bregma: 0.5 mm AP, 2 mm ML) for implanting an inverted gold pin as a reference electrode. A second rectangular craniotomy was made over the Cortex/SC region (Bregma: -3.5-3.8 mm AP, 0.5-1 mm ML), leaving the dura mater intact. The window was covered with silicone elastomer (Kwik-Sil, World Precision Instruments). The next day, Kwik-Sil was removed and the well around the craniotomy was constantly filled with ACSF throughout the whole recording session. Extracellular recordings were obtained using a single shank acute linear 32-channel silicon probe (ASSY-37 H4 with probe tip sharpening, Cambridge Neurotech) connected to an RHD 32-channel amplifier board and RHD2000 USB Interface Board (Intan Technologies). Behavioral readouts, such as running and eye/pupil movement together with the timing of optogenetic/visual stimuli, were obtained simultaneously with the electrophysiological signal. Before recording, the tip of the electrode was coated with DiI (Invitrogen) to allow post hoc recording site location. To access the superficial SC, the probe was slowly inserted through the cortex at a speed of 1 μm sec^{-1} to a depth of ~ 1.7 mm using a stable micromanipulator (Luigs & Neumann Motorized, Germany). The electrode was left in place for 30 min before starting to record. Data were sampled at 20 kHz using Labview 2017 (National Instruments). Mice were head-fixed using a custom-manufactured clamp. Spike-sorting was performed with Kilosort 2 (https://github.com/cortex-lab/Kilosort) (*59*). The automatic template of Kilosort 2 was manually curated on Phy2.

Setups for head-fixed in vivo recordings

For awake behaving experiments, two similar setups were used, with the difference that one was coupled to a custom-built multiphoton setup, and the other allowed for silicon probe/neuropixels recordings. In short, mice were head-fixed while awake using a custom-manufactured clamp (for imaging: connected to a three-axis motorized stage (8MT167-25LS, Standa)) and could run freely on a custom-designed spherical treadmill (20-cm diameter). Running behavior was recorded by a pair of ADNS-3080 (iHaospace, Amazon) optical flow sensor modules, focused with 25 mm lenses (AC127-025-AB-ML, Thorlabs) on a small patch at orthogonal locations of the Styrofoam ball and illuminated by an 850 nm LED. The

alternating sensor readout was controlled at 50 frames/s by an Arduino Uno running custom scripts. The 4 signal channels from the sensor were linearly mapped to movement speed in the forward, sideways and rotational axes based on regular calibration with synchronous measurement of image translations and rotation at the ball's apex. Eye and body movements were recorded at 50 fps with infrared illumination (850 nm) with a Camera (acA1920-150um, Basler) and an 18-108 mm macro zoom objective (MVL7000, Thorlabs) for multi-photon imaging or a fixed focal length objective for electrophysiology (Edmund Optics, f = 50 mm #59-873), pointed at the right side of the mouse via an infrared mirror. Eye position and saccades were determined post-hoc as previously reported (*37*), by first labeling eight points around the pupil with DeepLabCut (*60*), which were fitted to an ellipse, and the center position was transformed to rotational coordinates. Fast eye position changes of more than 45 ° s^{-1} and at least 3 ° amplitude on a 0.7 s median filtered trace were defined as saccades. The ellipse area in mm^2 was determined as pupil size.

Visual stimuli were projected by a modified LightCrafter (Texas Instruments) at 60 Hz (Multiphoton setup: DLP Lightcrafter evaluation module; e-phys setup: DLP LightCrafter 4500, Texas Instruments), reflected by a quarter-sphere mirror (Modulor) below the mouse and presented on a custom-made spherical dome (80 cm in diameter) with the mouse's head at its center. For imaging experiments, a double bandpass filter (387/480 HD Dualband Filter, Semrock) was positioned in front of the projector to minimize light contamination during imaging. In both setups, the blue LED in the projector was replaced by UV (LZ1-00UB00-01U6, Osram) and in addition, in the multi-photon setup, the green LED was replaced by a cyan LED (LZ1-00DB00-0100, Osram) not to interfere with the Calcium imaging wavelengths. The reflected red channel of the projector was used for synchronization and captured by a trans-impedance photo-amplifier (PDA36A2, Thorlabs) and digitized. Stimuli were designed and presented with Psychtoolbox-3 (*61*), running on MATLAB 2020b (MathWorks). Stimulus frames were morphed on the GPU using a customized projection map and an OpenGL shader to counteract the distortions resulting from the spherical mirror and dome. In both setups, the dome allows the presentation of mesopic stimuli from circa 100 ° on the left to ca. 135 ° on the right in azimuth and from circa 50 ° below to circa 50 ° above the equator in elevation.

Visual stimuli

All visual stimuli were generated using Psychtoolbox (Version 3) (*61*), running in MATLAB (Mathworks) on Microsoft Windows 10 systems. In between dynamic stimuli presented in randomized order, the screen was set to a homogeneous gray (green & UV light) at scotopic level for at least 30 s. To determine behavioral coupling, these stimuli were interspersed with 5 min gray screens, i.e., at visual baseline.

Visual local flash and optogenetics stimulation

Prior to starting the experiment, the visual field was scanned with a dark disk with 10 ° radius to determine the approximate location of receptive fields. We used this location to present a white or dark disk of the same radius. The visual local flash was interleaved in time with the laser burst of the same length, stimulating optogenetically vLGN. The duration of the laser and

visual stimulation was 200 ms (Fig. 2E-G, I, Fig. SB-F) or 1 sec (Fig. 2H, Fig. S4A). We used 13 different equally spaced and offsets of the laser bursts relative to the start of the visual flash in the range [-1.5,1.5]*t_flash, where t_flash is the duration of the flash. The sequence of the offsets was randomized. The laser bursts were generated in Arduino Due (www.arduiono.cc) in pulses of 40 Hz, the start of each burst was triggered from the Matlab stimulus script. We used the laser SDL-473-XXXSFL-RA (Shanghai Dream Laser Technology Co. Ltd) with a peak wavelength at 473 nm and approximate power at the fiber tip of 2.5 mW/mm^2.

Full-field flash

For *in vivo* electrophysiology, full-field flashes of three different intensities (low, medium, and high) were presented in a random order. Each flash lasted 1 s. Fig. 5B shows neuron responses collected for the sequence of high-to-low intensity flashes for OFF responses. The ON responses are shown in Fig. S9H-J. To quantify the change in pupil area during the flashes mean pupil area before the flash onset was subtracted Δa was subtracted a line fitted to Δa 200 ms after the start of the flash. The value of the slope of the fitted line was used as an estimate of the speed of change of the pupil area. For the analysis in Fig. 5D, mice were defined as moving if their forward speed was larger than 5 cm/s, including 0.5 s before and after such intervals. In the remaining time, mice were defined as still. In bouton imaging, either dark or white 1 s full field flashes were presented from gray baseline at a pseudorandom interval of 5 to 10 s.

Shifting white noise

A shifting spatio-temporal white noise stimulus (*37*) was used, where a random binary checker pattern is shifted by a random fraction of the checker size. Checker size was 8 °, and the pattern update was at 12 Hz. The same stimulus pattern was presented in green and UV channels.

Sinusoidal checkers

The stimulus is analogous to the one used in (*62*) but developed in Matlab. A random checker pattern (8 ° per checker) was oscillating sinusoidally by 17 ° in the horizontal direction. Each recording contained 450 cycles. Up to two sessions were recorded per mouse; due to synchronization problems, some recordings could not be analyzed and were discarded from the analysis.

Chirp stimulus

To measure sensitivity to luminance dynamics, repeated sequences of luminance chirps, as reported previously, were used. The stimulus started at gray level, followed by a 1 s bright step and sinusoidal luminance changes over 8 seconds each, first with increasing amplitude at 2 Hz and then fixed full amplitude but frequency modulated (0 to 8 Hz).

Full field gratings

Sinusoidal gratings of 0.1 cycles per degree spatial frequency, and 2 Hz temporal frequency were presented at full contrast moving in 8 or 16 directions in randomized order. Gratings were presented stationarily for 3 s and then moved for 7 s in the current direction.

Moving bars

A dark bar with length spanning the screen and width of 25 ° was moved over gray background at 22.5 °/s in 8 directions perpendicular to the bar orientation for 7 s with 3 s interval between presentations.

Pseudosaccade stimulus

Vertical gratings with 0.08 to 0.25 cpd spatial frequency, or random checkerboard patterns with 4 to 12 ° visual angle checker size were presented on the screen. At pseudorandom intervals between 3 to 6 s the full screen texture moved in a random horizontal direction over 0.08 s by a median of 5 ° (3 to 30 °) visual angle. The distribution of such pseudosaccadic image shifts approximately matched those from actual saccades, as determined from population spontaneous saccade statistics.

Current Source Density Analysis

To confirm the location of the silicone probe during the *in vivo* recordings, current source density analysis (*63*, *64*) was applied. For this analysis, local flash stimuli that were at least 0.5 s after the laser burst were used. For each such repetition of the flash, CSD profile (*64*) was computed on the raw voltage recorded values in the interval [-0.1, 0.2] s around the flash onset and averaged over multiple repetitions. The channel of the silicone probe corresponding to the current sink is defined as the channel where the current flow is the smallest. The closest channel above with positive current flow is the source. The depth of the source channel was set to 300 μm; the depth of the remaining channels is derived relative to the source using the 25 μm spacing between the channels. The response magnitude (Fig. 2F) was computed as the variance of the CSD profile of each channel across time. The normalized response (Fig. 2G) is the variance across all channels after the variance before the onset of the flash was subtracted and normalized to the maximum.

The same procedure was applied to compute the CSD analyses around laser bursts but selecting laser burst onsets that were at least 0.5 s after a visual flash.

Responses to Saccades in SC

Saccades were identified as described above during the sinusoidal checker stimulus. The firing rate of each neuron was computed during [-0.2, 0.4] s around the start of a saccade by binning the spikes into 25 ms bins. We further performed the zeta-test (*65*) to identify responsive neurons (p-value $\leq$ 0.05). The difference in mean firing rate of the responsive neurons between Sham and TeLC groups (Fig. 5K) was computed using a permutation test (p-value = 0.001, observed difference = -1.32, effective size = -0.58).

Optokinetic reflex (OKR)

During the sinusoidally moving checker stimulus, the eyes follow the motion of the stimulus. Fig. 5C shows the azimuth position of the pupil during each repetition after subtracting the mean value across the cycle. Averaging all 450 repetitions resulted in the mean optokinetic

response to the stimulus. If two recordings per mouse were available, we used the OKR values only from the first recording.

Receptive fields

The receptive fields of the neurons were computed as a spike-triggered average of the shifting white noise stimulus. Specifically, we averaged a stack of 30 frames before every spike of a neuron to obtain its 3D RF. We used the method in (*37*) for parameterization of RFs. Briefly, after translating the 3D RF such that the point of the maximum variance was in the center, we then fitted the difference of the Gaussians. We used the ellipse corresponding to doubled standard deviations of the central Gaussian as the mask of the center of the RF, which we then applied to the 3D RF. Averaging the pixels within the mask we get the temporal traces displayed in Fig. S9D-E.

Visual Cliff Experiments

Behavior

The visual cliff paradigm we used evaluates the preference of untrained mice (Control (AAV5-hSyn-DIO-mCherry infected) and TeLC (AAV5-hSyn-FLEX-TeLC-P2A-dTomato infected) in an open field arena, to stay or not within the limits of an illusory platform. We build a black walled plexiglass box (W: 50 cm x L: 50 cm x H: 80 cm). At the top of the box, we added a transparent plexiglass (5 cm thick) with black walls extending up to 25 cm. The illusory platform (25 x 25 cm) was a paper-printed checkerboard pattern glued at the bottom of the transparent plexiglass. A black plexiglass border (W: 1cm x H: 0,5 cm) matching the outer limit of the illusory platform was added to the surface. Below the transparent plexiglass, all interior walls and bottom floor were covered with a high-contrast checkerboard pattern (2.5 x 2.5 cm sized black and white squares) so that all edges were aligned.

Whisker clipping

One day before experiments, mice were shortly anesthetized with Isoflurane (5 %) and vibrissae clipped next to the mystacial pad with surgical scissors. Once recovered, mice were returned to the maintenance cage.

Recording

A camera (Basler acA1920-150um) with a fixed focal length objective (Edmund Optics, f = 50 mm #59-873) was located above the middle point of the arena to cover all movements. Camera control and recordings were obtained using a custom-made script in Python. Each mouse was recorded for 30 min while freely roaming in the arena.

Analysis

The head and body were tracked using a custom-trained network in DeepLabCut (*60*). We used ear tags for the mouse trajectories as they were the most reliable tracking points in our setup. After 30 min of recording, the mice explored the full extent of the arena. For each recording, we measured the size of the arena in pixels and scaled all frames to 103 x 103 pixels for

consistency. For the analysis, we used only the first 15 min of the recording because control mice seemed to change their behavior after that time, learning that the cliff was illusory.

After rescaling the videos, the size of the video frames was 500 x 500 pixels. We define the platform offset as an exit zone at 600 pixels from the lower left corner of the arena. The cliff avoidance index (Fig. 5M) is computed as $AI = (t_{platform}-t_{cliff})/(t_{platform}+t_{cliff})$, where t is the time spent at the platform or cliff normalized by the area of these regions. To compute the avoidance index, we excluded 10 % of the area around the edge of the platform and 100 pixels around the edge of the platform and cliff (Fig. 5K). The platform exit (Fig. 5N-O) is the 2 s portion of the trajectory centered at the time of crossing the exit zone. The exit trajectory is at the boundary if it is within 200 pixels of the left or bottom edge of the arena otherwise, it is in the central region. Aborted exits (Fig. 5P-Q) are the trajectories when a mouse crosses the platform boundary from inside the platform and reverses the direction of the velocity normal to the platform boundary after crossing the boundary. The aborted trajectories are 4 s long and centered on the time of crossing the platform boundary. To avoid double counting of the same aborted trajectory, we skip 1 s after the detected event of the aborted exit. For statistical tests, we used the Wilcoxon Rank Sum test.

Analysis of visual local flash and optogenetics stimulation stimulus

Neuronal responses

By grouping the stimulus repetitions by the offset of the laser burst relative to the visual flash we could detect the effect of the visual and laser stimulation on the individual neurons (Fig. 2H-M). For each neuron, we performed the zeta-test (*65*) and a permutation test (*66*) with subsampling to identify neurons that were responsive to the visual or optogenetic stimulation. We decided to use both tests because they detect two complementary responses of a neuron to a stimulus: the zeta-test identifies neurons with event-locked responses, whereas the permutation test captures neurons whose mean firing rate was altered, including tonic changes of the firing rates, such as in the case of optogenetic stimulation of vLGN/IGL complex. We used the same threshold of the p-value = 0.01 for both of the tests to decide whether a neuron was responsive to stimulation. For the permutation tests for visual ON/OFF or optogenetic ON/OFF responses, the firing rate during the stimulus was compared to the baseline firing rate. The latter was estimated from random samples of 0.2 s intervals of the trials before the start of the visual flash or laser burst. *Visually responsive* neurons are defined as neurons that have either ON or OFF responses to the flash within 0.2 s after the start/end of the flash. A neuron is considered *optogenetically responsive* if it exhibits a change of the baseline firing rate during 0.2 s after the start or end of the laser burst or if its visual ON/OFF responses were altered in the presence of optogenetics, for which we used a permutation test to compare ON/OFF flash responses with ON/OFF responses when they overlapped with the laser burst. For analysis in Fig. 2I-M only neurons responsive to the visual flash and laser burst were selected.

To investigate the dynamics of the vLGN/IGL stimulation on the visual responses of neurons in SC we used the local flash stimulus when both the flash and the laser burst lasted for 0.2 s. Grouping the trials by the laser burst offsets, we computed the mean firing rate during the visual

flash as a function of the laser burst offset. In Fig. 2L, we collected responses from all neurons, normalized them such that the maximum response of a neuron across all laser offsets is unit, and finally computed the mean response among all neurons per laser offset, revealing the effect of optogenetic stimulation of vLGN/IGL on the visual responses in SC.

Behavior analysis

For behavior analysis during optogenetic stimulation, we used the stimulus for visual local flash and optogenetic stimulation with the duration of the flash and laser burst of 1 s. To remove the effect of the visual flash on the behavior, we selected only those trials of the stimulus where the laser offset preceded the visual flash. To study the effect of vLGN/IGL stimulation on locomotion, we collected the forward and sideways velocity values (Fig. 4B). For visualization, we subtracted the mean velocity values computed during 0.25 s before the onset of the laser burst and sorted the trials by the mean forward velocity during 0.5 s after the onset of the laser. Similarly, we collected the azimuth position of the pupil during optogenetic stimulation (Fig. 4C-D). For each trial, we computed the azimuth change (Δ az) by subtracting the initial azimuth position of the pupil estimated as the mean pupil azimuth during 0.25 s before stimulus onset and sorted the trials using the mean Δaz during 0.5 s after the laser onset. We also computed the velocity of the pupil during each trial (Fig. S7A, C) as a central difference of consequent pupil azimuth $v_t = (az_{t+1} - az_{t-1})/2$. Selecting the trials where velocity exceeded 14 °/s, we plot the velocity profile of the pupil during each trial and the mean velocity across all selected trials (Fig. S7A, C), as well as the change in pupil azimuth vs. its starting position computed as the mean pupil azimuth during 0.25 s before laser onset (Fig. 4D). To compute the change in pupil azimuth, we found the location *T* and the width *w* of the maximum peak in the pupil velocity profile and computed the change in azimuth as $\Delta az = az_{T-w/2} - az_{T+w/2}$. Additionally, we collected the values of the pupil diameter during the selected trials. Fig. 4E shows the mean pupil diameter computed during 0.25 s before and after laser offset; the difference between the two conditions was estimated using the Wilcoxon signed rank test ($p = 10^{-74}$).

***In vivo* terminal imaging and ROI segmentation**

Two-photon terminal imaging in superior colliculus was performed as described previously (*37*). In brief, ScanImage (Vidrio Technologies) on MATLAB 2020b (MathWorks) controlled a custom-built microscope using a pulsed Ti:Sapphire laser (Mai-Tai DeepSee, Spectra-Physics) set at wavelengths between 920 and 950 nm. The beam was expanded to underfill the back-aperture of the objective (×16 0.8-NA water-immersion, Nikon) and scanned through the tissue by a galvanometric-resonant (8 kHz) mirror combination (Cambridge Scientific) and a piezo actuator (P-725.4CA, Physik Instrumente) controlling the objective. Emission light was measured with GaAsP photomultiplier tubes (H10770B-40, Hamamatsu) following collection by a dichroic mirror (FF775-Di01, Semrock) and channel splitting (580 nm long-pass, FF580-FDi01, Semrock) as well as filtering (green: FF03-525/50; red: FF01-641/75; Semrock). The signals were then amplified by a TIA60 amplifier (Thorlabs) and digitized with a PXI system (PXIe-7961R NI FlexRIO FPGA, NI 5734 16-bit, National

Instruments). Average laser output power at the objective ranged from 38 to 125 mW (median of 75 mW). A FOV of 0.13–1.85 mm^2 (median of 0.77 mm^2) was imaged over 3–12 planes (median of 6 planes) with a plane distance of 10–45 µm (median of 28 µm) at a pixel size of 0.6–1.9 µm (median of 1.3 µm) and a volume rate of 4.2–9.5 Hz (median of 4.8 Hz). Each mouse was recorded in 1-9 (median of 7) imaging sessions on different days. In a subset of recordings (n = 15) in separate imaging sessions, the absence of substantial z-motion was verified by injecting 40 µl of Texas Red dextran (3000 MW, 14.3 mg ml^{-1}, diluted in saline, Thermo Fisher Scientific) s.c. and imaging brightly red labeled blood vessels at 980 nm (*67*).

Imaging data was motion corrected and ROI segmented with suite2p (v0.10.0)(*68*) followed by a manual curation step based on morphological and activity shape. Note that multiple axonal ROIs can originate from the same neuron. dF/F_0 was then estimated in MATLAB R2021a (MathWorks), as previously (*37*, *69*), by subtracting neuropil contamination with a factor of 0.5, defining F_0 baseline as the 8th percentile of a moving window of 15 s (*70*) and finally subtracting and then dividing the fluorescence trace by the median of the same 15 s window. The fluorescence signal-to-noise ratio was defined for each ROI by dividing the 99th percentile of the dF/F_0 trace ('signal') by the standard deviation of its negative values after baseline correction ('noise'). Only axonal segments with a fluorescence SNR ≥ 5 were included in further analysis.

In vivo axonal terminal imaging analysis

Imaging data analysis was done in MATLAB R2021a (MathWorks) with custom scripts. To estimate modulation by visual and behavioral stimuli, modulation indices were computed by $(F_{response} - F_{baseline}) / (F_{response} + F_{baseline})$, F being the average dF/F_0 value in a baseline or response window, respectively. For moving bar and grating stimuli, baseline window was defined as 1.5 s to 0.1 s before movement start, response window from 0.25 after stimulus start the end of the stimulus. For full field luminance modulation baseline was between 1.3 s before and until frequency modulation start, response as the time of frequency modulation presentation. For 0.5 s black or white full field flashes, baseline window was the second before flash onset, response window, the second following flash onset. For saccades and locomotion onset 1.5 s to 0.5 s before were used as baseline and the second following onset was used as response window. For pseudosaccade analyses, baseline window was defined as 0.5 to 0.1 s before and response window as 0.5 s following the pseudosaccade or saccade. Only saccadic events separated by at least 0.75 s from other saccadic events were included to avoid cross-contamination. Significance of modulation was determined by two-sided Wilcoxon signed-rank tests. Significance of correlations was determined by 5000 repeats of randomly shifting the behavioral trace between 120 s and 1200 s and computing correlations for shuffled datasets. Significance was then determined by calculating the proportion of shuffles with more extreme correlation values than the actual data. Boutons from either vLGN/IGL or retina were included in further analysis if they showed Bonferroni-corrected significant ($p < 0.001$) modulation or correlation to at least one of the up to 8 tested conditions. Note that not all recordings included all stimulus sections. These inclusion criteria removed 102833/322854 vLGN/IGL and 22646/101376 RGC overall recorded boutons from further analysis. Population synchrony was

determined as variance of the population mean divided by the population mean of individual bouton variance. Similarly, individual bouton variance explained was determined by z-scoring bouton activity, and computing 1 - variance of the mean subtracted activity. To determine direction selectivity and preferred directions, 1 - circular variance was used. To demonstrate preferred direction distribution (Figs. 3E and S5E), only boutons with significant direction tuning $p < 0.01$ (10000-fold shuffled direction label test) were plotted. To estimate retinotopic alignment of bouton responses maximal response latencies for mean responses to each bar direction was computed and bouton centroid locations were projected on the 1-dimensional axis with maximal bouton location (20 µm binned) to response latency correlation. To disentangle independent locomotion and pupil size contributions to bouton correlations, correlations to pupil size were separately computed for stationary periods (0.25 s window median filtered locomotion speed < 1 cm/s). Due to large sample sizes, comparisons between bouton populations yield arbitrarily high significances. In these cases, effect sizes r, defined as the Wilcoxon-signed rank z-statistic divided by the square root of the sample size, are reported alongside.

Euthanasia and histology

Mice were dosed with 750-1000 mg kg^{-1} mixture of ketamine/xylazine and transcardially perfused with PBS, followed by ice-cold 4 % paraformaldehyde (PFA) in PBS. Brains were carefully extracted and post-fixed overnight, cryoprotected with sucrose 30 %, and sectioned at 60 µm using a sliding microtome (Leica SM2010). Sections were collected in three series. The first series was used for signal amplification of the respective vector. Briefly, sections were incubated with PBST (Triton 0.3 %) solution containing 5 % donkey normal serum and one or more antibodies (goat Anti GFP, ab6673, Abcam, diluted 1:2000; rabbit anti-RFP, 600-401-379, Rockland, diluted 1:1000) overnight at 4 °C, followed by secondary fluorescent antibodies (Donkey anti-goat-488, ab150129, Abcam, diluted 1:1000; Donkey anti-rabbit-594, R37119, ThermoFischer, diluted 1:1000) at room temperature for 1 h. Sections were mounted on slides and coverslips with custom-made mowiol.

Confocal microscopy

Brain sections were imaged with a Nikon CSU-W1 spinning disk confocal microscope. All images were processed with FIJI (ImageJ).